PHASE LIGHT CURVES FOR EXTRASOLAR JUPITERS AND SATURNS

Ulyana A. Dyudina,[1,2] Penny D. Sackett,[2] and Daniel D. R. Bayliss[3]

Research School of Astronomy and Astrophysics, Mount Stromlo Observatory, Australian National University,
Cotter Road, Weston Creek, Canberra, ACT 2611, Australia

S. Seager

Observatories of the Carnegie Institution of Washington, 5241 Broad Branch Road NW, Washington, DC 20015

Carolyn C. Porco

CICLOPS, Space Science Institute, 3100 Marine Street, Suite A353, Boulder, CO 80303-1058

and

Henry B. Throop and Luke Dones

Southwest Research Institute, 1050 Walnut Street, Suite 426, Boulder, CO 80302

ABSTRACT

We predict how a remote observer would see the brightness variations of giant planets similar to those in our solar system as they orbit their central stars. Our models are the first to use measured anisotropic scattering properties of solar system giants and the first to consider the effects of eccentric orbits. We model the geometry of Jupiter, Saturn, and Saturn's rings for varying orbital and viewing parameters, using scattering properties for the (forward scattering) planets and (backward scattering) rings as measured by the *Pioneer* and *Voyager* spacecraft at 0.6–0.7 μm. Images of the planet with and without rings are simulated and used to calculate the disk-averaged luminosity varying along the orbit; that is, a light curve is generated. We find that the different scattering properties of Jupiter and Saturn (without rings) make a substantial difference in the shape of their light curves. Saturn-sized rings increase the apparent luminosity of a planet by a factor of 2–3 for a wide range of geometries, an effect that could be confused with a larger planet size. Rings produce asymmetric light curves that are distinct from the light curve that the planet would have without rings, which could resolve this confusion. If radial velocity data are available for the planet, the effect of the ring on the light curve can be distinguished from effects due to orbital eccentricity. Nonringed planets on eccentric orbits produce light curves with maxima shifted relative to the position of the maximum phase of the planet. Given radial velocity data, the amount of the shift restricts the planet's unknown orbital inclination and therefore its mass. A combination of radial velocity data and a light curve for a nonringed planet on an eccentric orbit can also be used to constrain the surface scattering properties of the planet and thus describe the clouds covering the planet. We summarize our results for the detectability of exoplanets in reflected light in a chart of light-curve amplitudes of nonringed planets for different eccentricities, inclinations, and azimuthal viewing angles of the observer.

Subject heading: methods: data analysis — planetary systems — planets: rings —
planets and satellites: individual (Jupiter, Saturn) — scattering

1. INTRODUCTION

Modern space-based telescopes and instrumentation are now approaching the precision at which reflected light from extrasolar planets can be detected directly (Jenkins & Doyle 2003; Walker et al. 2003; Green et al. 2003; Hatzes 2003). Since 1995, more than 100 extrasolar planets (or exoplanets) have been detected indirectly by measuring the reflex motion of their parent star along the line of sight (radial velocity or Doppler method). One of these radial velocity planets, Gl876b, has been confirmed by measuring the parent star motion on the sky (astrometry; Benedict et al. 2002), and a second, HD 209458b, by measuring the change in parent star brightness as the planet executes a partial eclipse of its host (transit photometry; Charbonneau et al. 2000; Henry et al. 2000). Three exoplanets have now been detected by transit photometry (Udalski et al. 2002a, 2002b, 2003) and then confirmed with Doppler measurements (Konacki et al. 2003, 2004; Bouchy et al. 2004). It is expected that in the next decade, as photometric techniques are improved from both the ground and in space, detection of the reflected light from exoplanets will prove useful not only in expanding the number of known exoplanets but also in detailing their characteristics.[4]

Reflected light from an exoplanet can be detected in two ways. First, with precise, integrated photometry, one can search for temporal variations in the combined parent star and exoplanet light curve due to the planet changing phase in reflected light throughout its orbit, in the same way as the Moon changes phase. The vast majority of the light comes from the star itself, with a small constant thermal contribution for giant planets, but if the periodic variations due to light reflected by the planets can be extracted from the total phase light curve, the

---

[1] NASA Goddard Institute for Space Studies, 2880 Broadway, New York, NY 10025.

[2] Planetary Science Institute, Australian National University, ACT 0200, Australia.

[3] Victoria University of Wellington, New Zealand.

[4] Reviews and references on extrasolar planets and detection techniques can be found at http://www.obspm.fr/encycl/encycl.html.

planetary phase as a function of time can be deduced. Furthermore, since the planet's light and the starlight need not be spatially resolved, relatively distant planetary systems and planets at small physical orbital radii can be studied.

Already, ground-based observations of known short-period exoplanets have been conducted to search for reflected light signatures in high-resolution spectroscopy (Charbonneau et al. 1999; Collier Cameron et al. 2002; Leigh et al. 2003a, 2003b). To date, no signature of reflected light has been detected, but because the orbital phase is known from radial velocity measurements, these nondetections constrain the gray geometric albedo p of the planet for an assumed phase curve, orbital inclination, and planetary radius. For the assumed parameters of τ Boo b, HD 75289b, and the innermost planet of υ And, nondetections seem to imply that $p < 0.4$ (Collier Cameron et al. 2002; Leigh et al. 2003a, 2003b).

Second, with sufficient spatial resolution, direct imaging can resolve the planet and the star in space, so that the projected planetary orbit can be tracked simultaneously with the measurement of the planet's phases in reflected light. To be detected, planets must be at orbital distances large enough to be easily resolved from their parent star and yet close enough that the reflected brightness is large enough to be detected against the background. Consequently, the first extrasolar planets to be detected directly in this way are likely to be giants orbiting relatively nearby stars (at tens of parsecs) at intermediate semimajor axes (1–5 AU; Clampin et al. 2001; Lardière et al. 2004; Trauger et al. 2003; Krist et al. 2003; Codona & Angel 2004; Dekany et al. 2004).

Direct imaging can yield both the orbit and the luminosity of the planet simultaneously and thus yield robust detections. Although direct exoplanet imaging from either the ground or space may not be available for several years, our model light curves can be used for planning future observations of spatially resolved planets in reflected light.

The potential of exoplanet detection in reflected light and the possibility of detecting planetary rings is demonstrated by the number of works published in the last few years. Seager et al. (2000) modeled the atmospheric and cloud composition and simulated the light curves for close-in giant planets with various cloud coverages. Sudarsky et al. (2003) modeled clouds and spectra for extrasolar planets at different distances from the star. Barnes & Fortney (2004) modeled transit light curves for a planet with rings. Arnold & Schneider (2004) simulated light curves for planets with rings of different sizes, assuming planets with isotropically scattering (Lambertian) surfaces and rings with isotropically scattering particles, and provided a discussion of the possibility of ring presence at different stages of planetary system evolution.

Our model, however, is the first to use the *observed anisotropic scattering* of Jupiter, Saturn, and Saturn's rings and the first to calculate light curves for eccentric orbits. We find that anisotropic scattering yields light curves that are substantially different from those assuming Lambertian planets and isotropically scattering rings and thus is more likely to give an accurate description for extrasolar planets similar to Jupiter and Saturn.

In § 2 we describe our model. In § 3 we present our light curves for nonringed exo-Saturn and exo-Jupiter planets on an edge-on circular orbit, for variously oriented oblate exo-Saturns and for a ringed planet (with Saturnian scattering properties) at variously inclined circular orbits. In addition, we model a nonringed exo-Saturn, an exo-Jupiter, and a Lambertian planet on eccentric orbits. In § 4 we discuss the uncertainties

of our model and the detectability of the light curves by modern and future instruments. Conclusions are presented in § 5.

2. MODEL

We model the reflected brightness of an exo-Jupiter or exo-Saturn by tracing how light rays from the central star are reflected by each position on the planet. We then produce images (maps with a resolution of 16–200 pixels across, depending on the acceptable error level) of the planet and its rings for different geometries. The light rays from the star illuminating the planet are assumed to be parallel, consistent with both star and planet being negligible in size compared with the star-planet distance. The reflected rays collected by the observer are assumed to be parallel, consistent with a remote observer. The model includes reflection from the planet and rings and the rings' transmission and shadows but does not incorporate second-order effects such as ring shine on the planet or planet shine on the rings. We account for the planet's oblateness in some of our simulations by using the 10% oblateness of Saturn as an example.

The planetary reflected brightness in our model is derived from the data as an average brightness integrated along the planet's spectrum, weighted by the wavelength-dependent transmissivity of the *Pioneer* red filter, which is nonzero in the range 0.595–0.720 μm. Our notation matches that of most observational papers on Saturn and Jupiter. To compare our results with those from the models of Arnold & Schneider (2004), we list both our and their parameter names in Table 1.

Figure 1 demonstrates the geometry of a ringed planet on a circular orbit defined by the angles listed in Table 1. Besides the angles shown in Figure 1, which define the geometry of the planet as a whole, the scattering brightness of each position on the planet's or ring's surface depends on three angles: the phase angle α, the incidence angle via its cosine μ_0, and the emission angle via its cosine μ, as defined by the surface scattering phase function $P(\mu_0, \mu, \alpha)$. We obtain $P(\mu_0, \mu, \alpha)$ for Jupiter, Saturn, and the rings from the data as described in the subsections below.

2.1. *Reflecting Properties of Jupiter, Saturn, and Rings*

Figure 2 shows the scattering phase function for a given geometry, used in our model to describe surfaces of Jupiter, Saturn, and its rings. The normalized brightness of a point on the surface is plotted versus scattering phase angle α:

$$P(\mu_0, \mu, \alpha) \equiv I(\alpha, \mu_0, \mu)/(F\mu_0), \tag{1}$$

where $F\mu_0$ is the "ideal" reflected brightness of a white, isotropically scattering (Lambertian) surface, μ_0 is the cosine of the incidence angle measured from the local vertical, and $F(\pi$ sr) is the solar flux at the planet's orbital distance. In our notation, $\alpha = 0°$ indicates backscattering and $\alpha = 180°$ indicates forward scattering. Note the logarithmic scale of the ordinate and the large amplitudes of the phase functions. Lambertian scattering with reflectivity 0.82 (matching the observed Saturn's full-disk albedo at opposition) is shown as a horizontal solid line for comparison. We also indicate, for the same ring opacity, albedo, and geometry, the ring phase function used by Arnold & Schneider (2004), which assumes isotropically scattering particles. Figure 2 shows reflected light only for the geometry in which the Sun is 2° above the horizon ($\mu_0 = 0.035$) and the observer moves from the Sun's location ($\alpha = 0°$) across the

TABLE 1
PARAMETERS USED IN MODELING

This Work	Arnold & Schneider (2004)	Quantity
A, B		Coefficients of the Backstorm law
A_{HG}		Coefficient for Jovian phase function
a, a_1		Semimajor axis of the planet's orbit (AU)
D_P		Planet-star distance (km)
E		Eccentric anomaly (polar angle parameterization)
e		Eccentricity
F	γ	Intensity of a white Lambertian surface[a] (W m^{-2} sr^{-1})
g_1, g_2, f		Parameters of Henyey-Greenstein function
I	$L_p, I_R, I_T, L_{ps}, L_{pr}$	Intensity (or brightness, or radiance) of the surface (W m^{-2} sr^{-1})
i	i	Inclination of the orbit (0°: face-on; 90°: edge-on) (deg)
L_P		Luminosity of the planet[b] in reflected light
L_*		Luminosity of the star[b]
M		Mean anomaly (time parameterization)
p		Full-disk albedo,[b] $L_P/(\pi R_P^2 F)$
$P(\mu_0, \mu, \alpha)$		Scattering phase function of the surface
R		Star's magnitude in R band
R_P	r_p	Equatorial radius of the planet (km)
r_{pix}		Pixel size (km)
V		Star's magnitude in V band
α	α	Phase angle (deg)
δt		Temporal shift of light-curve maximum from pericenter (days)
ϵ		Planet's obliquity (deg)
Θ	$\phi = \Theta - 90°$	Orbital angle (±180°: minimum phase; 0°: maximum phase) (deg)
μ_0, μ	μ_0, μ	Cosines of the incidence and emission angle
ω		Argument of pericenter (90°: observed from pericenter, −90°: from apocenter) (deg)
ω_r		Observer's azimuth relative to the rings (deg)

[a] $F(\pi$ sr) is the incident stellar flux at the planet's orbital distance (which is also sometimes called F but has W m^{-2} units, unlike our intensity F measured per unit solid angle).

[b] The "red" or "blue" optical properties are the convolution of the planet's (or the ring's or the solar) spectrum with the wavelength-dependent transmissivity of the *Pioneer* filter (which is nonzero between 0.595 and 0.720 μm for the red filter and between 0.390 and 0.500 μm for the blue filter).
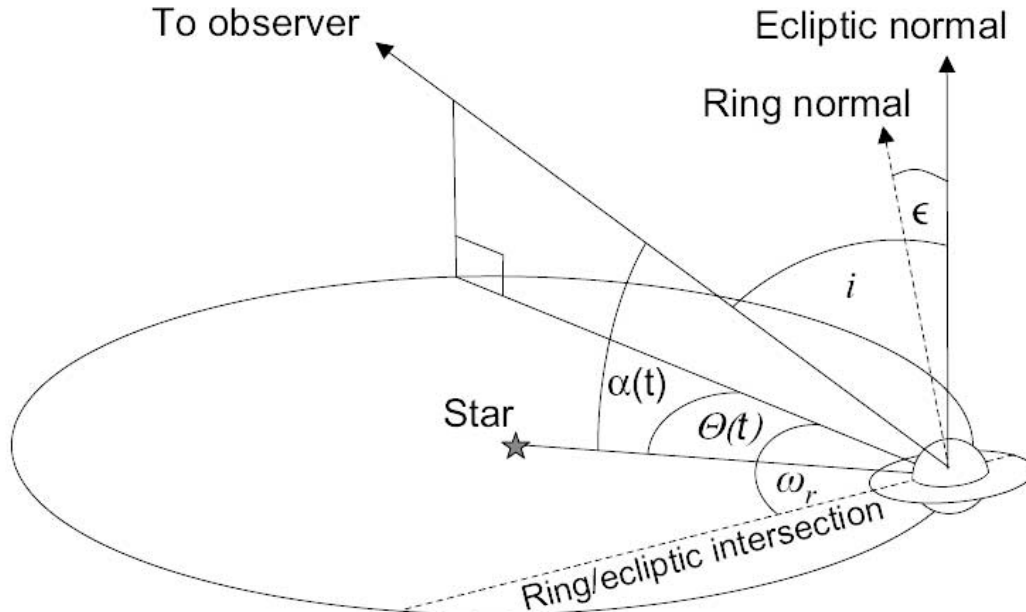

FIG. 1.—Angles defining the geometry of a ringed planet on a circular orbit observed from a large distance. Dashed lines show the normal to the ring plane and the line of intersection of the ecliptic with the ring plane. The observer's azimuth relative to the rings, ω_r, is positive when the rings are tilted from the ecliptic toward the observer, is negative when the rings are tilted from the ecliptic away from the observer, and changes from −90° to 90°. We do not consider other possible values of $\omega_r = \pm(90°-180°)$ because these orientations produce light curves symmetric to those with $\omega_r = \pm(0°-90°)$ $\omega_r = \pm0°$. For a nonringed planet, the geometry is fully determined by the inclination i and the orbital angle $\Theta(t)$. For a ringed planet, the geometry is fully determined by i, $\Theta(t)$, ω_r, and the obliquity ϵ.
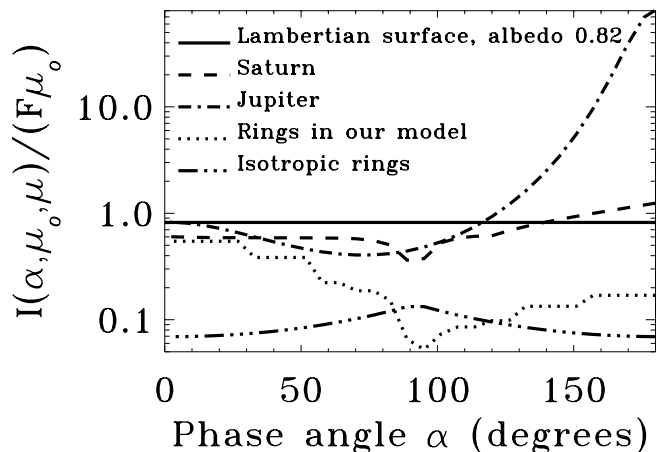
FIG. 2.—Our model scattering phase functions for a Lambertian surface, Saturn, Jupiter, and Saturn's rings and the phase function for rings consisting of isotropically scattering particles used by Arnold & Schneider (2004). The phase functions are plotted for a single sample geometry: μ_0 is fixed (the Sun is $2°$ above the horizon), while the observer moves in the plane that includes the Sun and the zenith. The wavelengths correspond to visible red light (0.6–0.7 μm).

FIG. 3.—Our fit of the Henyey-Greenstein function (*solid line*; $g_1 = 0.8$, $g_2 = -0.38$, $f = 0.9$, and $A_{HG} = 2$) to the *Pioneer 10* data (P10), published as Tables IIa and IIb of Tomasko et al. (1978), and to the *Pioneer 11* data (P11), published as Tables IIa and IIb of Smith & Tomasko (1984). The data represent belts (*dark stripes*) and zones (*bright stripes*) on Jupiter observed with the red (0.595–0.720 μm) and blue (0.390–0.500 μm) filters.

zenith toward the point on the horizon opposite the Sun ($\alpha = 178°$). We used different methods to obtain $P(\mu_0, \mu, \alpha)$ for Jupiter, Saturn, and the rings from *Pioneer* and *Voyager* data.

2.1.1. *Jupiter*

For Jupiter we fitted a simple four-parameter analytical function (two-term Henyey-Greenstein function) to the published data,

$$P(\mu_0, \mu, \alpha) \approx A_{HG}[fP_{HG}(g_1, \alpha) + (1-f)P_{HG}(g_2, \alpha)] \quad (2)$$

(Tomasko et al. 1978; Tomasko & Doose 1984). The coefficient A_{HG} is fitted to match the amplitude of the observed phase function. The individual terms are Henyey-Greenstein functions representing forward- and backward-scattering lobes, respectively:

$$P_{HG}(g, \alpha) \equiv \frac{1 - g^2}{(1 + g^2 + 2g\cos\alpha)^{3/2}}, \quad (3)$$

where α is the phase angle, $f \in [0, 1]$ is the fraction of the forward versus backward scattering, and g is g_1 or g_2; $g_1 \in [0, 1]$ controls the sharpness of the forward-scattering lobe, while $g_2 \in [-1, 0]$ controls the sharpness of the backward-scattering lobe.

Figure 3 shows our fit of the Henyey-Greenstein function to the data points from the *Pioneer 10* and *11* images (Tomasko et al. 1978; Smith & Tomasko 1984). This fitted function also reproduces the full-disk albedos observed by Karkoschka (1994, 1998) at the wavelengths corresponding to the red passband of *Pioneer*. *Pioneer* images taken with broadband blue (0.390–0.500 μm) and red (0.595–0.720 μm) filters show surface locations on Jupiter with different properties. In particular, Tomasko et al. (1978) and Smith & Tomasko (1984) have indicated two types of locations: the belts, usually seen as dark stripes on Jupiter (Fig. 3, *crosses*), and the zones, usually seen as bright stripes on Jupiter (Fig. 3, *plus signs*). The relative calibration
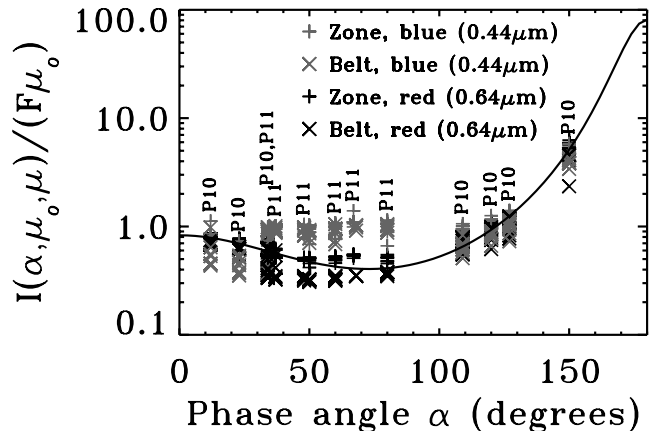
between *Pioneer 10* and *Pioneer 11* data is not as well constrained as the calibration within each data set. If we accept the calibrations given in Tomasko et al. (1978) for *Pioneer 10* and those given in Smith & Tomasko (1984) for *Pioneer 11*, our model curve better represents the observations in the red filter (*black data points*) than in the blue. The *Pioneer 11* blue data at moderate α in Figure 3 seem to be systematically offset from the *Pioneer 10* points, which may be a result of relative calibration error. Consequently, we do not model the blue wavelengths.

In addition to *Pioneer* data, images of Jupiter from a variety of angles were taken by *Voyager*, *Galileo*, and *Cassini*, although we are not aware of any published data of the scattering phase functions for the Jovian surface.[5] Data for $\alpha > 150°$ do not exist because these directions would risk pointing spacecraft cameras too close to the Sun. Our derived light curves are not severely affected by our extrapolation for $\alpha > 150°$, however, since when the forward scattering is important, the observed crescent is small, and the reflected light phase curve undergoes its minimum.

2.1.2. *Saturn*

The scattering phase function and albedo of Saturn are represented by the Backstorm law, which was used by Dones et al. (1993) to fit observations of Saturn's scattering:

$$\frac{I}{F} = \frac{A}{\mu}\left(\frac{\mu\mu_0}{\mu + \mu_0}\right)^B, \quad (4)$$

where A and B are coefficients that depend on the phase angle α. The coefficients are fitted by Dones et al. (1993) to *Pioneer 11* phase function tables, which were produced by the multiple-scattering model of Tomasko & Doose (1984). We averaged the coefficients published by Dones et al. (1993) separately for zones and belts through *Pioneer*'s blue and red filters. Table 2 gives the resulting coefficients; Figure 2 displays the red filter curve only. Figure 4 demonstrates the

---

[5] One of us, U. A. D., plans to work on obtaining the spectral phase functions from *Cassini* nine-filter visible images in the immediate future.

TABLE 2
COEFFICIENTS FOR THE BACKSTORM FUNCTION FOR SATURN

Phase Angle α	$0°$	$30°$	$60°$	$90°$	$120°$	$150°$	$180°$ [a]
A (red, 0.64 μm).....................	1.69	1.59	1.45	1.34	1.37	2.23	3.09
B (red, 0.64 μm).....................	1.48	1.48	1.46	1.42	1.36	1.34	1.31
A (blue, 0.44 μm).................	0.63	0.59	0.56	0.56	1.69	1.86	3.03
B (blue, 0.44 μm).................	1.11	1.11	1.15	1.18	1.20	1.41	1.63

NOTE.—Coefficients for the Backstorm function for Saturn are averaged between belt and zone values published in Table V of Dones et al. (1993).

[a] The coefficients at $\alpha = 180°$ are not constrained by observations and were estimated by linearly extrapolating the coefficients at $120°$ and $150°$.

difference between the blue and red phase functions for Saturn. The values for the blue curve are 1.5–2 times smaller, indicating that Saturn is darker in blue wavelengths because of higher absorption by photochemical hazes.

2.1.3. *Saturn's Rings*

The ring brightness in reflection (illuminated side) and transmission (unilluminated side) is provided by a physical scattering model of the ring. This model calculates multiple scattering within the rings using a ray-tracing code. The model ring is populated with macroscopic bodies of size 1 m, with optical depth and albedo profiles chosen to match those of Dones et al. (1993). The model reproduces well the brightnesses observed by *Voyager 1* and *2*. We use the code to predict ring brightness at geometries not observed by *Voyager*, bin the output into a look-up table, and then use the table to produce the ring images.

The ring brightness at each point is a function of three angles (α, μ, and μ_0), the optical depth, and the albedo. Because of data volume restrictions, we have binned output in rather large steps, which depend on parameter values. These steps are clearly seen in the ring phase function in Figure 2 (*dotted line*).

2.2. *Full-Disk Albedo*

To produce light curves of the fiducial exoplanets that we model, images of the planet for a set of locations along the orbit are generated. For each image, we integrate the total light

coming from the planet and the rings (if any) to obtain the full-disk (or geometric) albedo $p(\alpha)$:

$$p(\alpha) = \frac{\sum_{\text{pix}} I(\mu, \ \mu_0, \ \alpha) r_{\text{pix}}^2 / F}{\pi R_P^2}, \qquad (5)$$

where r_{pix} is the pixel size and R_P is the planet's radius. The full-disk albedo is the planet's luminosity L_P normalized by the reflected luminosity of a Lambertian disk with the planet's radius at the planet's orbital distance, illuminated and observed from the normal direction:

$$p \equiv L_P / (\pi R_P^2 F). \qquad (6)$$

2.3. *Eccentric Orbits*

In addition to modeling light curves from ringed planets traveling in circular orbits, we also model light curves of nonringed planets moving in eccentric orbits. Although most of the planets in the solar system orbit the Sun with low eccentricities, the extrasolar planets detected to date display a wide range of eccentricities.[6] As can be seen in Figure 5, the geometry of an ellipse introduces an additional parameter, in addition to inclination, in the observer's azimuthal perspective of the system. This parameter is the argument of pericenter, ω, which is the angle (in the planet's orbital plane) between the ascending node line[7] and pericenter (Murray & Dermott 2001).

To model the reflected light as a function of time, we calculate the angular position of the planet and the planet-star separation over a complete period using a solution to Kepler's equation: $M = E - e \sin E$, where M is the mean anomaly (a parameterization of time), E is the eccentric anomaly (a parameterization of the polar angle), and e is the eccentricity. Kepler's equation is transcendental and cannot be solved directly. Applying the Newton-Ralphson method[8] to Kepler's equation, we obtain the iterative solution for the planet's position:

$$E_{i+1} = E_i - \frac{E_i - e \sin E_i - M_i}{1 - e \cos E_i}. \qquad (7)$$

3. RESULTS

The shape of the phase light curve depends on many parameters: the planet's orbit, its geometry relative to the observer, the planet's oblateness, the scattering properties of the
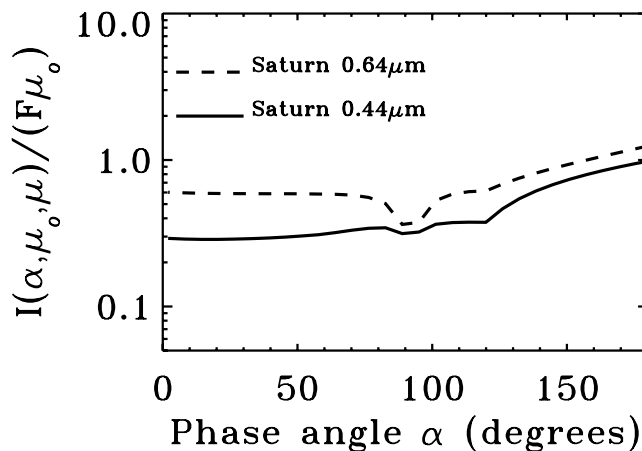
FIG. 4.—Scattering phase functions for Saturn in the red (0.595–0.720 μm) and blue (0.390–0.500 μm) passbands adopted from Dones et al. (1993) for the same scattering geometry as in Fig. 2. The optical depth at the sample point on the rings (1.7 times Saturn's radii from the planet's center) is 2.3; the albedo of the ring particles is 0.56. The ring is observed from the illuminated side.

[6] Eccentricities of extrasolar planets are listed at http://exoplanets.org/almanacframe.html.

[7] The reference plane is formed by the observer's line of sight and its normal in the ecliptic plane, which is also the ascending node line.

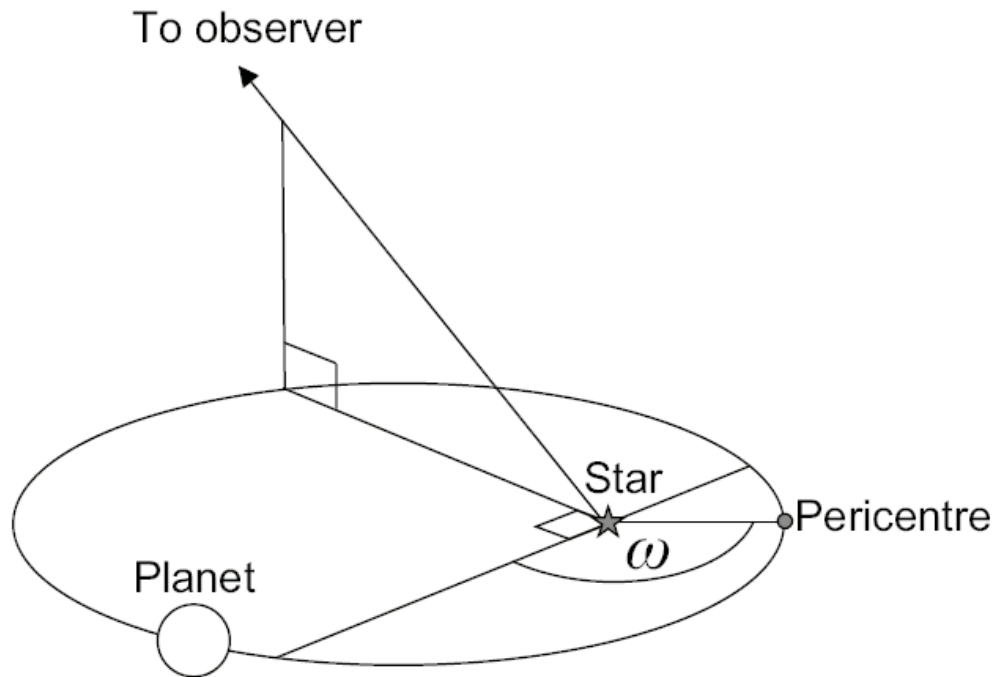[8] The application of the Newton-Ralphson method to Kepler's equation is described in Murray & Dermott (2001).

Fig. 5.—Argument of pericenter, ω, an additional angle needed to define the geometry of a nonringed planet on an eccentric orbit.

planet's surface, and the presence and geometry of rings. To study whether these signatures can be identified unambiguously in the light curve, we modeled several geometries for the planetary system, i.e., different orbital eccentricities e for nonringed planets and different ring obliquities ϵ relative to the ecliptic for ringed planets on circular orbits. For each of these cases, we modeled a variety of observer locations, i.e., different orbital inclinations i as seen by the observer and different azimuths ω of the observer relative to the orbit's pericenter or to the rings (ω_r). In what follows, we compare light curves for these differing geometries and discuss whether or not different geometric effects can be distinguished from one another.

3.1. Light Curves for Jupiter versus a Ringless Saturn

We first compare spherical ringless exoplanets with different surface reflection characteristics on circular orbits. Figure 6 compares edge-on light curves for a ringless Saturn, a Jupiter, and a Lambertian planet. The reflected planet luminosity is normalized by the incident stellar illumination to obtain the full-disk albedo p as described in equations (5) and (6). The model planets have identical radii; the curves differ only because of the different surface scattering of the three planets.

The full-disk albedo can be converted to the planet's luminosity L_P as a fraction of the star's luminosity L_* for a planet of equatorial radius R_P at an orbital distance D_P,

$$L_P/L_* = (R_P/D_P)^2 p. \qquad (8)$$

For example, for Saturn at 1 AU, $(R_P/D_P)^2 \approx 1.6 \times 10^{-7}$. The abscissa of Figure 6 indicates the azimuthal angle of the planet in its orbital plane (the orbital angle Θ of Fig. 1), starting at minimum planet phase ($\Theta = -180°$). The plot can be transformed into a time-dependent light curve simply by dividing Θ by $360°$ and multiplying by the planet's orbital period.

The light curve for Jupiter peaks much more sharply at full phase ($\Theta \approx 0°$) than the light curves of Saturn or the

Lambertian planet because of the sharp backscattering peak in Jupiter's scattering phase function (at $\alpha \approx 0°$ in Fig. 2). Near zero phase ($\Theta \approx \pm 180°$) in Figure 6, Jupiter is more luminous than the other two models because of the large forward scattering from its surface ($\Theta \approx 180°$) in Figure 2. Such differences in phase functions are commonly attributed to larger particle size in the main cloud deck on Jupiter. For example, Tomasko et al. (1978) suggest particle sizes larger than 0.6 μm to explain the forward scattering.

3.2. Light Curve for Oblate Planets versus Spherical Planets

Next we examine the effect of planet oblateness. Saturn's equatorial radius is 10% larger than its polar radius. This oblateness of Saturn (6% for Jupiter) makes the planet appear larger when looking at the pole than when looking at the
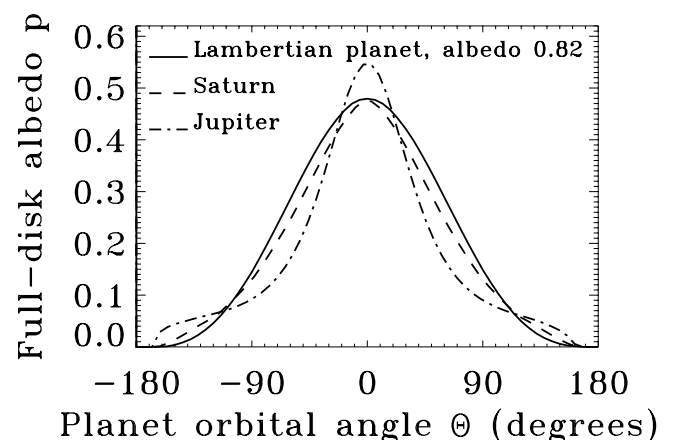

Fig. 6.—Comparison of light curves for a spherical Jupiter, a spherical Saturn, and a spherical Lambertian (isotropically scattering) planet, assuming the planets are ringless and have the same radii R_P. The planets differ only in their surface scattering properties. Albedos are shown for visible red light (0.6–0.7 μm).
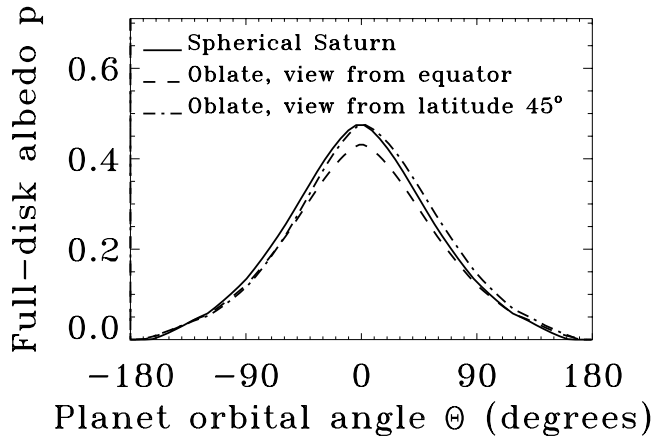
FIG. 7.—Comparison of light curves for a spherical and a 10% oblate planet with Saturn's surface properties. Planets have the same equatorial radii and are ringless. The orbit is observed edge-on ($i = 90°$). The planets are rotating "on their sides" ($\epsilon = 90°$). The albedos shown are for visible red light (0.6–0.7 μm).

equator, which affects the light curves. Figure 7 compares light curves for a spherical planet, a 10% oblate planet viewed at its equator, and a 10% oblate planet viewed at 45° latitude.

All three sample planets have the same equatorial radius and scattering properties as Saturn. We display light curves for an edge-on orbit ($i = 90°$) of a planet rotating "on its side" ($\epsilon = 90°$), because this geometry emphasizes the effects of oblateness in the reflected light. The differences among the curves are created by differences in the observer's azimuth relative to the planet's equator, an angle analogous to ω_r but measured with respect to the equatorial plane rather than the ring plane. Observing the planet at the equator decreases the cross section of the planet and thus decreases the amplitude of the curve. Observing the planet at the pole yields a curve indistinguishable from the solid curve for a spherical planet; this

is not shown in Figure 7. Observing the planet at 45° latitude produces a small asymmetry in the curve.

3.3. Light Curve for a Ringed Planet

Rings have a large effect on the light curves of planets. To describe the geometry of ringed planetary systems, two more parameters are required. If we assume a fixed radial density distribution for the rings, the geometry becomes sensitive to the ring obliquity ϵ (the angle between the ring and ecliptic planes) and to the azimuth of the observer relative to the rings ω_r (see Fig. 1).

Figure 8 shows an example light curve for $i = 55°$, $\epsilon = 27°$, and $\omega_r = 25°$, which is a convenient geometry to demonstrate different ring effects in one light curve. The cartoon on the right of Figure 8 displays images of Saturn at several positions on the orbit. The plot on the left shows the light curve for a ringed planet (Fig. 8, *plus signs*) compared with the curve for a ringless planet (Fig. 8, *solid curve*) with the same geometry. The ~10% spread of the points in the ringed light curve is partially due to the large steps in the ring reflection table (steps are also seen in Fig. 2) and should be treated as a model uncertainty. For a large fraction of the orbit, the presence of rings increases the luminosity of the planet ($\Theta < -20°$) because the observer is able to view more reflecting surface. However, for $0° < \Theta < 100°$, rings shadow part of the planet, producing a lower luminosity than that for the nonringed planet. More importantly, the ringed light curve is asymmetric, which makes it distinguishable from any light curves of a nonringed planet on a circular orbit.

The variety of light curves for a Saturn-like planet for different geometries is illustrated in Figure 9, from which one can learn several lessons. First, rings generally increase the amplitude of the light curves by a factor of 2–3. An amplitude increase due to rings could be partially confused with effects due to a larger planet size or larger albedo. This ambiguity may be resolved spectrally because the spectrum of rings should be
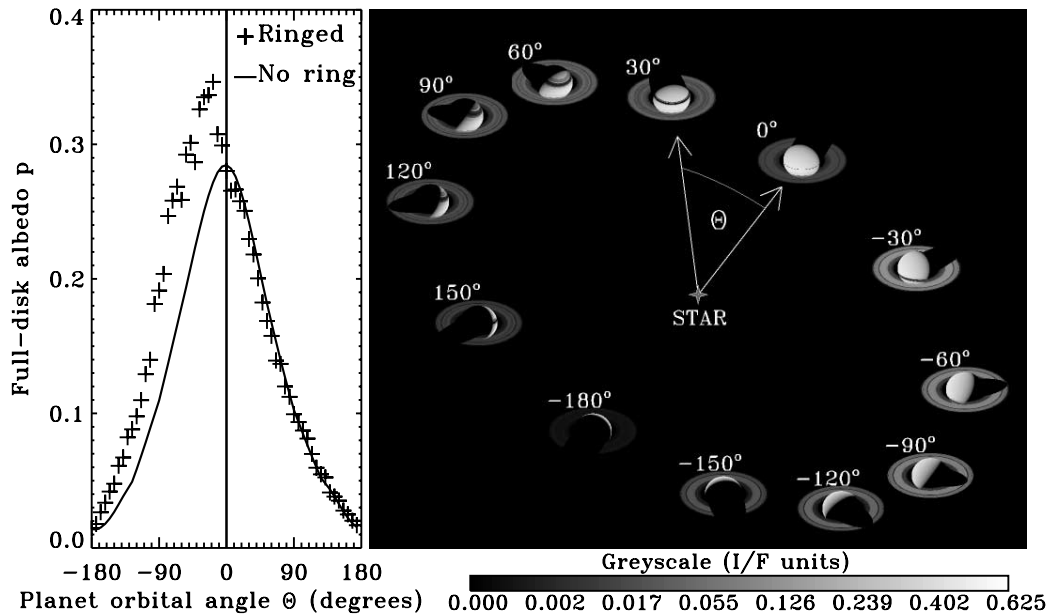

FIG. 8.—Effect of Saturn's rings if observed from 35° above the orbital plane ($i = 55°$). In this example, the obliquity of Saturn's rings is $\epsilon = 27°$. *Right*: Observer's azimuth on the ecliptic separated from the intersection of the ring and ecliptic planes by $\omega_r = 25°$. Values of Θ are indicated next to each image. The brightnesses of the images in the cartoon are given in units of I/F, as indicated on the nonlinear gray-scale bar. *Left*: Light curves for a ringless planet (*solid curve*) and for a ringed planet (*crosses*).
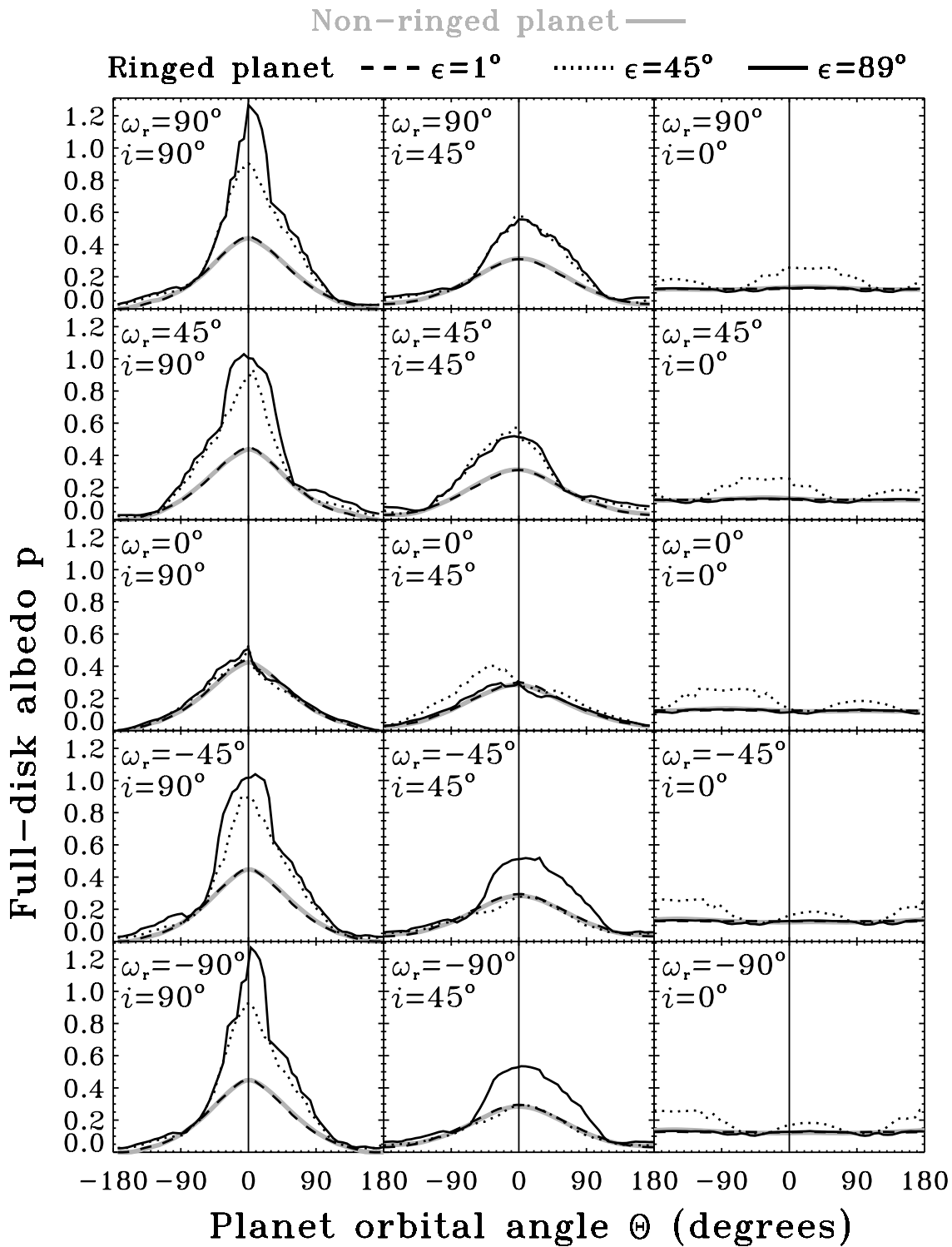
FIG. 9.—Light curves for Saturn for different geometries. Different ring obliquities ϵ are shown on each subplot as black curves of different line type. A curve for a spherical planet without rings is shown in gray. Each column corresponds to a different orbital inclination i. Each row corresponds to a different azimuth ω_r of the observer relative to the rings.

rather flat, whereas the planetary atmosphere is expected to be dark at a set of prominent gaseous absorption bands.

The second lesson is that light curves for a ringed planet are asymmetric. There are two types of asymmetry. The first, which is potentially easier to detect, is the offset of the curve's maximum relative to $\Theta = 0°$, the maximum of the light curves for a ringless planet (Fig. 9, *vertical lines*). The offset of the maxi-

mum itself occurs in a rather small fraction of the plots. However, since the entire curve is asymmetric, the effect would be detectable as an overall deviation from the simple symmetric curves likely to be used to fit the first detections of reflected light. If radial velocity data exist for a planet, the exact timing of the $\Theta = 0°$ point would be measurable. In this case, a shifted maximum in the light curve would yield direct evidence of the rings.

The shifted maximum is a strong photometric signature that was also noted in the ring simulation of Arnold & Schneider (2004) as a "ϕ-shift." We stress, however, that other processes may be capable of producing such a ϕ-shift. Similar, although probably smaller, shifts may be induced by a seasonal brightness variation on the planet. Note, however, that none of the giant planets in the solar system have pronounced seasonal brightness variations. The ϕ-shifts could also be produced by a global asymmetry of the brightness distribution over the planet or by the planet's oblateness (see § 3.2). Again, spectroscopy may help to resolve the ambiguity between asymmetries caused by rings and those caused by processes on the planet surface. Abrupt asymmetric changes in the fine structure of the light curve give a more robust indication of the rings than a ϕ-shift, but resolving such detail would require another order of magnitude in instrument sensitivity.

The third lesson that we can draw from Figure 9 is that in the case of face-on orbits (*right column*), both radial velocity observations and precise photometry would give no signal for a nonringed planet. A ringed planet, on the other hand, typically produces a double brightness maximum, as the rings are illuminated first from the observer's side and then from the back side during the orbit (*dotted curve*). Double maxima can also be produced in eccentric orbits, but these have different fine structure (see § 3.4). We note, however, that a double peak may be generated by seasonal variations or by an uneven brightness distribution at the planet's surface.

3.4. *Light Curve for a Planet on an Eccentric Orbit*

As an example of the effect orbital eccentricity may have on the light curve of a planet in reflected light, Figure 10 shows light curves for a ringless planet with the orbital characteristics of exoplanet HD 108147b and the equatorial radius of Jupiter. HD 108147b provides an interesting test case because some of the very first planets to be detected in reflected light will be "close-in" and yet on eccentric orbits (HD 108147b has $e = 0.498$ even though its semimajor axis is small at $a = 0.104$ AU). We compare Lambertian, Jovian, and Saturnian scattering properties in Figure 10 (*top*) to demonstrate the effect of anisotropic scattering, but the primary motivation for Figure 10 is to show the effect of orbital eccentricity.[9] The orbital parameters assumed for Figure 10 are those determined for HD 108147b by precise radial velocity measurements (Pepe et al. 2002). We assume the planet to be 10% oblate, as is Saturn. We plot the light curve over one complete orbit, beginning at pericenter.

The light curves of Figure 10 can be rescaled easily for a planet with the same orbital eccentricity but different semimajor axis a_1 by multiplying the luminosity by $(a/a_1)^2$ and multiplying the time axis by the ratio of the orbital periods $(a_1/a)^{3/2}$. Since the inclination of the orbital plane cannot be determined from radial velocity measurements, we display in Figure 10 (*bottom*) light curves for inclinations between $i = 90°$ (edge-on) and $0°$ (face-on). Here we use Jovian scattering as our test case because it produces the most prominent inclination features in the light curves. The argument of pericenter ω (see Fig. 5) can be derived from radial velocity measurements. For HD 108147b, $\omega = -41°$, which means that we are fortunate to be at the azimuth at which the fullest planet phase $\Theta = 0°$ (Fig. 10, *vertical line*) is separated from pericenter by only

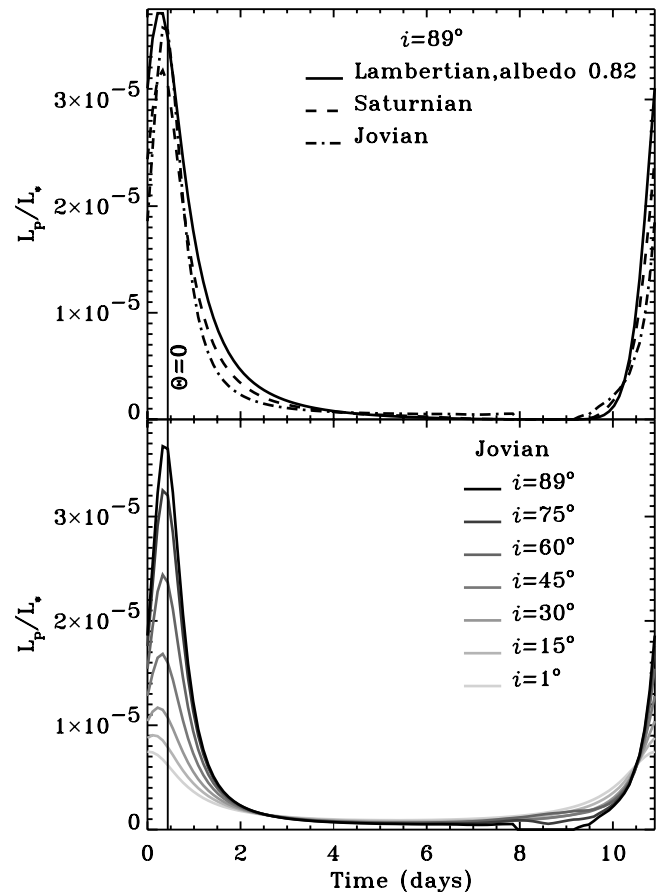Fig. 10.—Light curves for a planet on an eccentric orbit (orbital characteristics of exoplanet HD 108147b: $a = 0.104$ AU, $e = 0.498$), assuming Jupiter's equatorial radius and 10% oblateness. The planet's luminosity L_P is normalized by the star's luminosity L_* and plotted vs. time. The argument of pericenter is $\omega = -41°$. The corresponding time of the planet's maximum phase $\Theta = 0°$ (*vertical line*) is ~0.4 days after pericenter (which defines time zero). *Top*: Comparison of edge-on light curves for planets with Jovian, Saturnian, and Lambertian surfaces. *Bottom*: Comparison of different orbital inclinations from face-on to edge-on orientations ($i = 1°–89°$, respectively).

$41°$. With such a geometry, the phase-induced and eccentricity-induced maxima on the light curve amplify one another. As a result, the amplitude of the curve for the edge-on case is about 3.5×10^{-5}, nearly 5 times larger than for the face-on case, in which only the orbital distance variation matters.

Figure 11 illustrates the importance of the argument of pericenter in determining the light curves of a given system measured by the observer. The light curves assume the same orbit as in Figure 10, but the argument of pericenter is now set to $\omega = 60°$ rather than $-41°$. Such a change in the observer's position causes a threefold decrease in the amplitude of the edge-on ($i = 89°$) light curves.

For the $\omega = 60°$ geometry, a secondary peak located close to pericenter appears on the edge-on Jovian light curve. If the planet is less forward scattering than Jupiter (e.g., Saturn or a Lambertian planet), the second peak does not appear. The $i = 89°$ and $75°$ light curves display a sharp trough in which the amplitude of reflected light is reduced almost to zero. This trough is due to the planet showing no phase ("new moon") at this point of its orbit.

3.4.1. *Temporal Shift of Light-Curve Maximum δt*

The position of the light-curve maximum relative to the pericenter (the temporal shift, δt, in Fig. 11) can yield important

---

[9] We do not expect a close-in planet such as HD 108147b to have clouds similar to those of Jupiter or Saturn, and we do not attempt to model in detail the scattering properties of close-in planets. Our scattering models are more appropriate for planets covered by water or ammonia clouds.
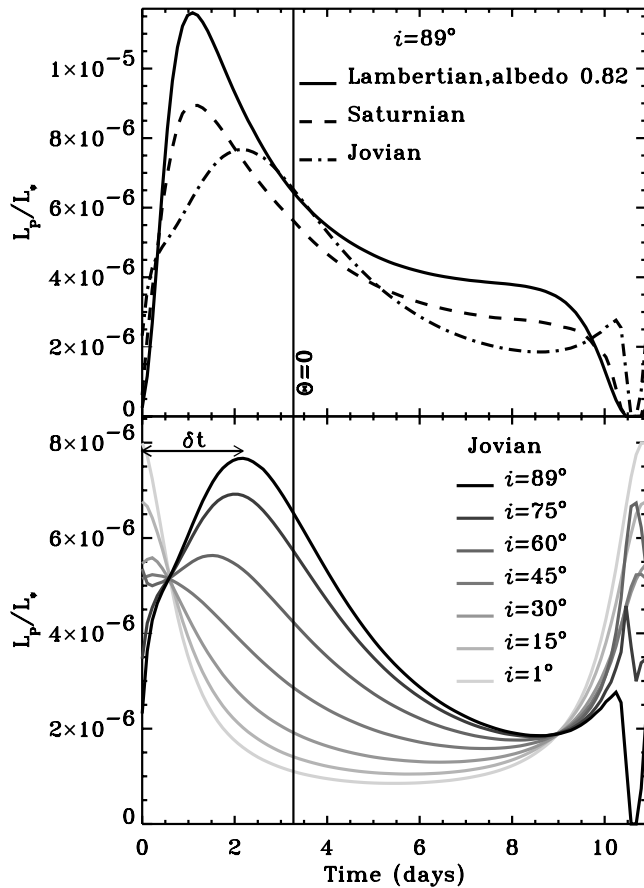
tering planet. For example, in Figure 11, a 2 day δt can be produced only by the Jovian planet.

To learn whether the observed δt is high enough to restrict atmospheric scattering, one can examine the three columns of Figure 12, which summarize scattering from Jovian (*left column*), Saturnian (*middle column*), and Lambertian planets (*right column*). As an example, if $e = 0.4$, $\omega = 60°$, and the observed temporal shift is 25% of the orbital period (*green*; δt values), only the left column, corresponding to Jovian scattering, displays green anywhere along the $\omega = 60°$ vertical line; thus, only strongly backscattering planets like Jupiter could be consistent with such an observation. Note, however, that this restriction on atmospheric scattering may be contaminated by ring effects, large-scale bright patches on the planet's surface, or seasonal variation of the cloud coverage.

3.4.2. *Contrast: Amplitude of Light-Curve Variations*

The contrast, or difference between the maximum and minimum amplitude of the light curve, gives a measure of the degree of variability that the planet's reflected light displays. It is this variation that new-generation space- or ground-based photometers may be able to detect if they can achieve the required levels of precision.

We plot the light-curve contrast for all possible orbital orientations in Figure 13. These contour maps display the degree of contrast for various orbital inclinations and arguments of pericenter at given eccentricities. Note that the backscattering peak of Jupiter's surface makes the planet much darker at low orbital inclinations than a Saturnian or Lambertian planet. For a given orientation, the more eccentric orbits show much higher contrast than do the circular orbits, although the amount of contrast depends strongly on both the inclination and the argument of pericenter. At high eccentricities, favorable geometries (such as $i = 90°$ and $\omega = -90$) can increase the contrast by approximately 5 times over those of less favorable orientations.

4. DISCUSSION

4.1. *Uncertainties*

Our model provides a rather accurate description of reflected light curves for Jupiter and Saturn. The largest uncertainties are due to the lack of observations at large phase angles (forward scattering at $\alpha > 150°$) for the surfaces of Jupiter, Saturn, and its rings. The extrapolations we have made to the phase functions could result in a factor of a few error in the brightness at these angles, at which the light curves have their minimum. The contrast in the highest amplitude light curves (edge-on orbits) is constrained to within a few percent by high spectral resolution, ground-based observations of Saturn and Jupiter. In our study, the uncertainty of these maximum amplitudes is 10%–20% because the brightness of a planet varies with wavelength by about this amount within the 0.6–0.7 μm spectral range (Karkoschka 1998).

Reflectivity of the rings may be in error by as much as 50% because many geometries, especially those for face-on ring illumination and face-on ring observation, are not constrained by observations. New observations by the *Cassini* spacecraft will fill this gap in the data. Another source of ring error is the scattering properties of the coarse grid in the tabulated ring (see § 2.1.3). This grid-induced noise is usually below 30% of the ring's luminosity.

Rings around close-in, short-period exoplanets may be unlikely because of tidal disruption and in any case can consist

FIG. 11.—Light curves for the same eccentric orbit as in Fig. 10, except that the argument of pericenter is $\omega = 60°$. The temporal shift δt is marked for the Jovian nearly edge-on ($i = 89°$) light curve.

constraints on the inclination of the orbit and the cloud cover of the planet. First, as the inclination increases, the maximum moves from pericenter toward the time of the maximum phase $\Theta = 0°$; i.e., δt increases. Unlike the amplitude of the curve, which is also an indicator of inclination, δt cannot be produced by altering the planet's size or albedo. However, this interpretation can be confused by the unknown strength of backscattering at the planet's "surface" (see Fig. 11, *top*).

Figure 12 summarizes the sensitivity of δt to the inclination of the orbit and different atmospheric scattering properties. If radial velocity data exist for the planet, then the orbital eccentricity e and argument of pericenter ω are known, and the shift, indicated by color coding in Figure 12, is observable. The orbital inclination i (Fig. 12, *ordinate*) is generally not known, unless transit or astrometric data are available.

Our method of constraining the orbital inclination i using Figure 12 is achieved by matching the measured δt values with those along the vertical line corresponding to the known ω on the plot with the appropriate eccentricity e, as measured by radial velocity techniques. An ambiguity remains because of the unknown scattering properties of the planet's surface, which can sometimes be resolved by comparing the detailed shape of the light curves.

Second, δt may also serve to constrain the surface properties of the planet. In some cases, a lower limit may be put on the strength of backscattering from the planet's surface. For any scattering surface, the maximum possible δt occurs on the edge-on orbit ($i = 90°$); see examples in Figure 11 (*top*). The largest δt values are possible only from a strongly backscat-
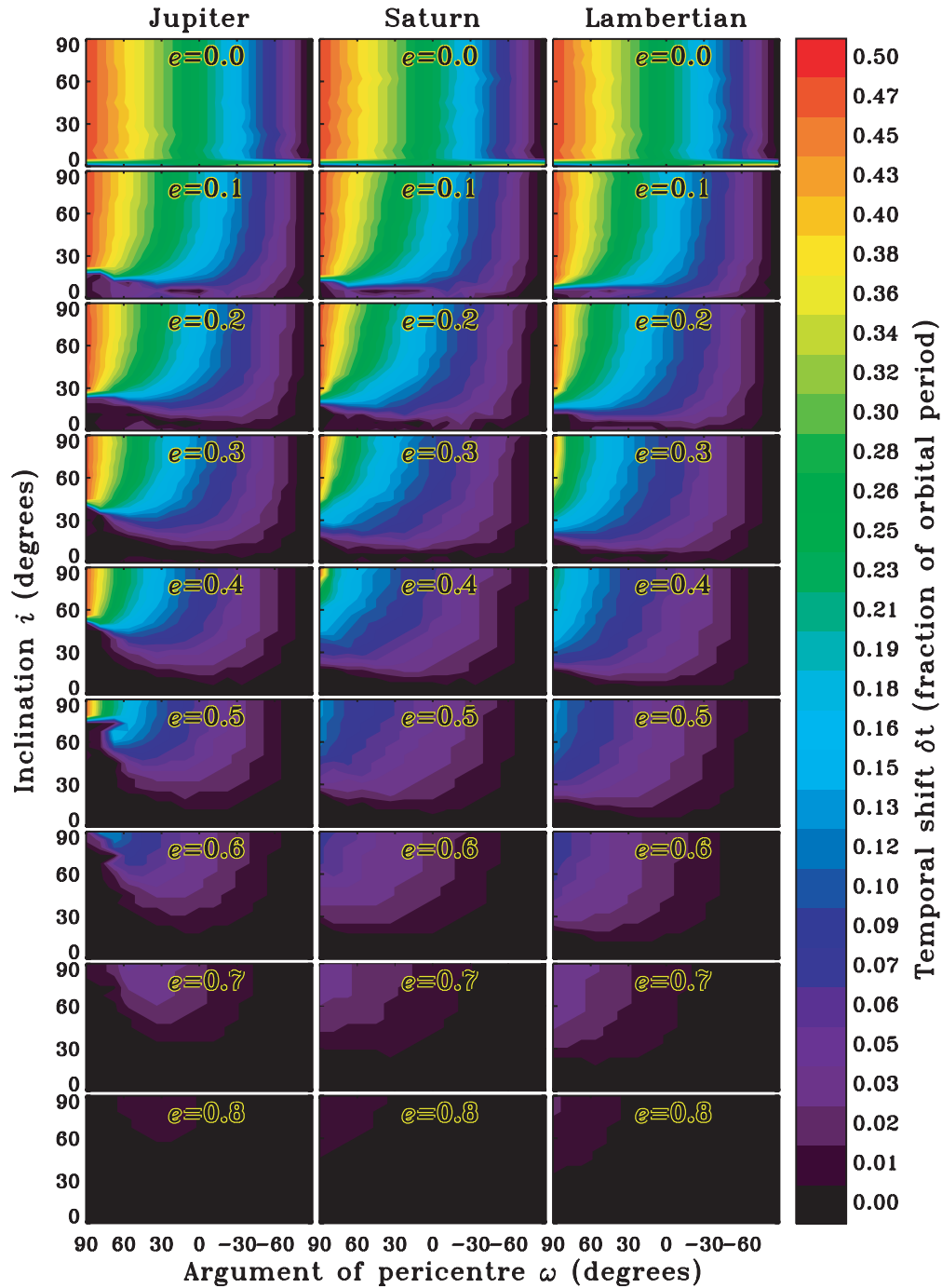
Fɪɢ. 12.—Summary of the temporal shift δt of the light-curve maximum from pericenter for eccentric orbits at different observational geometries for planets with Jovian (*left column*), Saturnian (*middle column*), and Lambertian (*right column*) scattering properties. Shifts are measured as a fraction of the orbital period. Each planet is assumed to be 10% oblate. The eccentricity of the orbit increases from the top row of subplots to the bottom row. The viewing geometry is described by the orbital inclination and argument of pericenter, plotted on the ordinate and abscissa, respectively, of each subplot.

only of rock. (Saturn's rings are 99% ice.) Ice rings are stable against evaporation outside ∼7 AU for solar-type stars (Mekler & Podolak 1994). Rocky rings may be several times darker than ice rings but would still backscatter for geometric reasons.

The total ring size for an exoplanet may be very different from that of Saturn's rings, which would have a large effect on the ring luminosity. We refer the reader to the work of Arnold & Schneider (2004), who investigate ring size effects.

The optical depth of rings around an extrasolar planet may also differ substantially from that of Saturn's. It is important to note that when a ring has an optical depth greater than about

3–5, the brightness of the illuminated side and thus the amplitude of the light curve become insensitive to further increases of optical depth. More than half the area of Saturn's rings has an intermediate optical depth of 0.5–3, which can be considered neither optically thin nor optically thick. These optical depths cause the unilluminated side of Saturn's ring to be quite bright. If the rings are optically thin, some asymmetry due to shadows will remain, but the light-curve asymmetry due to the different sides of the ring will decrease.

Applying our model light curves to the bodies of short-period ($a < 0.1$ AU) giant exoplanets, whose bright light curves are the
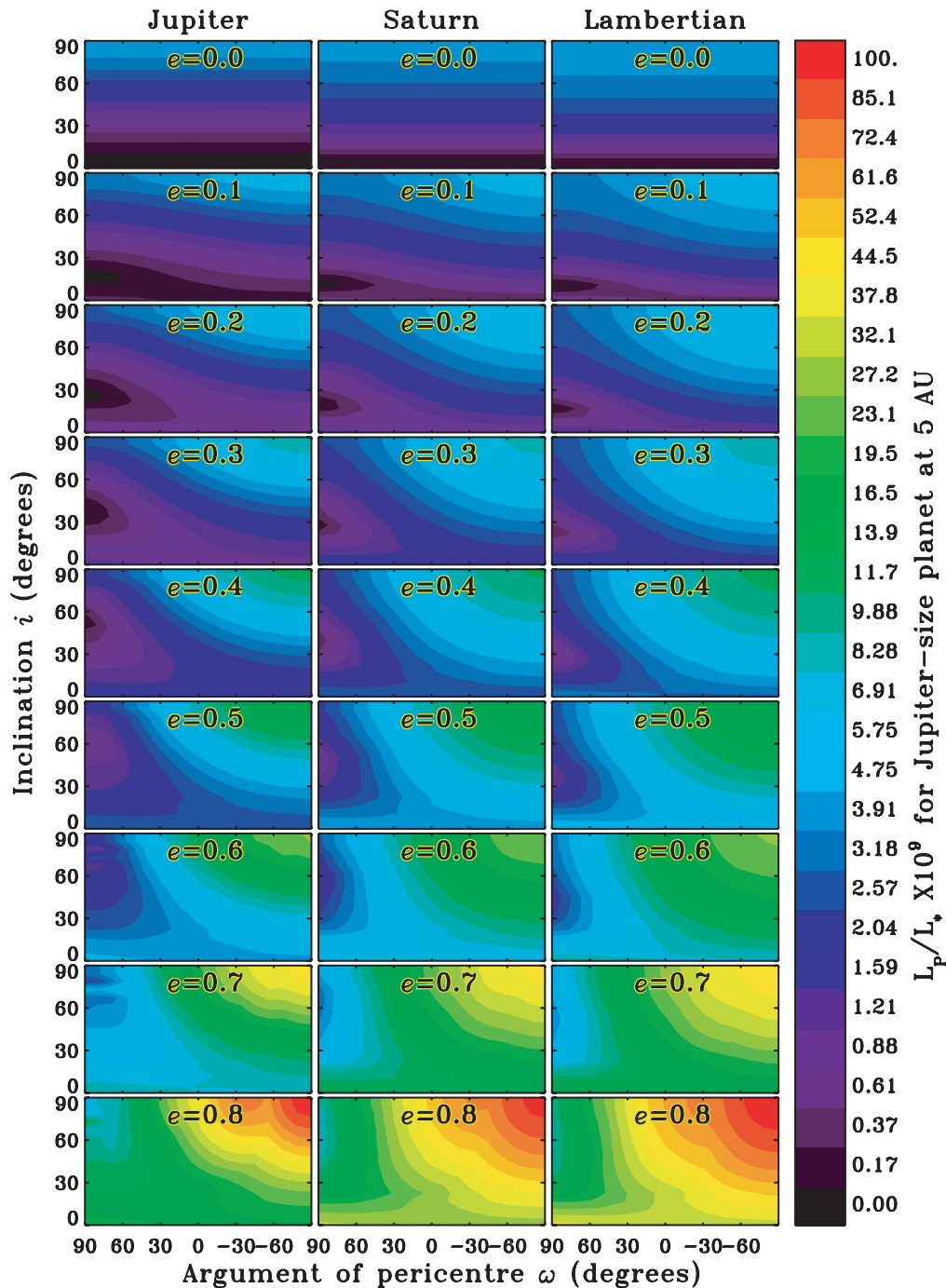
Fig. 13.—Summary of light-curve variability amplitudes, or contrast, for eccentric orbits at different observational geometries for Jovian (*left column*), Saturnian (*middle column*), and Lambertian scattering properties (*right column*) with surface albedo 0.82, which matches Saturn's observations at opposition (see § 2.1). Planets are assumed to be 10% oblate.

most observable, has a number of complications related to chemistry. The clouds on these exoplanets are expected to be composed of solid Fe, $MgSiO_3$, Al_2O_3, and other condensates that are stable at high temperatures (Burrows & Sharp 1999; Seager et al. 2000), rather than the water and ammonia ices predicted for solar system giants (Weidenschilling & Lewis 1973). Thus, clouds may be darker, and the corresponding light-curve amplitudes may be several times smaller. It is possible that forward- and backward-scattering maxima typical of Jupiter and Saturn could occur for cloud-covered exoplanets even if their cloud composition is different. Remarkably, no direct spectral

signature of ammonia or water ice particles is found on Jupiter except in small weather patches that cover only a few percent of Jupiter's area (Simon-Miller et al. 2000; Baines et al. 2002), which may be due to the coating of the condensate particles by photochemically produced materials. Whether the photochemistry on extrasolar giant planets could alter the surface of cloud particles is beyond the scope of this paper, but any direct comparison of clouds made of pure silicate on short-period extrasolar planets, for example, with the clouds made of pure ammonia on Jupiter and Saturn, is probably oversimplified. The most important parameter in determining the brightness of a planet is

the presence or absence of clouds, which depends on poorly known (even for Jupiter and Saturn) vertical atmospheric circulation. Detection or nondetection of a light curve with the expected amplitudes would be most indicative of such cloud presence.

4.2. Prospects for Detection by Modern Instruments

What are the prospects for detection of reflected light from exoplanets? Our model light curves can serve as a guide. The amplitudes in Figures 6–9 can be converted to measurable units of fractional luminosity L_P/L_* by using equation (8) and compared with expected observational sensitivities. For a typical extrasolar planet discovered to date, for example, with a radius equal to Jupiter's (71,400 km) and an orbital semimajor axis in the range 0.3–3 AU, a conversion factor between 2.5×10^{-4} and 2.5×10^{-8} multiplying the order-of-unity light-curve amplitudes displayed in Figures 6–9 yields L_P/L_*. For convenience, we have scaled the amplitudes in the summary plot in Figure 13 to a Jovian analog with a semimajor axis equal to 5 AU. The ratio L_P/L_* depends inversely on the square of the planet's orbital distance, independent of the star's distance to the observer.

Short-period giant planets are the easiest targets for detection by precise, spatially unresolved photometry because they are well illuminated by the star. As discussed in § 3, light curves for such planets may differ from those we present here for Jupiter and Saturn because their hotter temperatures (and possibly different evolution as a result of migration) alter their atmospheres and clouds and thus their surface scattering properties. Nevertheless, our model light curves do provide a first-order approximation for an exoplanet covered by ammonia or water clouds, which the models of Sudarsky et al. (2000) predict outside about 1 AU around solar-type stars and at considerably smaller radii around stars of later spectral class.

The ability of precise space-based photometers such as *MOST* (which has been launched but has no survey capability) and *Kepler* (for which the launch is planned in 3–4 years and which will have survey capability) to detect reflected light from extrasolar planets depends on the signal-to-noise ratio (S/N) of the observations and thus the apparent brightness of the target parent star. Precisions approaching 10^{-6} are expected for bright $V \leq 6$ stars with *MOST* (Green et al. 2003; Walker et al. 2003) and $\sim 7 \times 10^{-5}$ for faint $R = 12$ stars with *Kepler*[10] (Jenkins & Doyle 2003; Koch et al. 2000; Jenkins et al. 2000; Remund et al. 2002).

Within a fiducial survey volume of radius 30 pc, in which a solar-type star would have $V \leq 7.2$ and $R \leq 6.9$, *MOST* and *Kepler* would thus be able to provide measurements with precisions of $\sim 2 \times 10^{-6}$ and $\sim 6 \times 10^{-6}$, respectively, except when they are dominated by instrumental or stellar noise. Actual sensitivities may differ somewhat since for short-period planets the S/N may be increased by repeated observations over several orbits, and longer period planets may be confused with fluctuations in stellar luminosity on the order of 10^{-5} (Jenkins & Doyle 2003). As Figure 13 shows, gas giants with semimajor axes $a \leq 0.2$ and Jovian, Saturnian, or Lambertian scattering properties should exhibit detectable signatures above 10^{-5} for a wide range of viewing angles and orbital eccentricities. If, on the other hand, albedos of close-in planets are as low as those

predicted by Sudarsky et al. (2000), such planets will be considerably more difficult to detect with *MOST* and *Kepler*.

Our models are particularly relevant to the direct, spatially resolved imaging planned for future space instruments such as the Terrestrial Planet Finder Coronagraph (TPF-C) or ground-based adaptive optics systems, including those planned for the Extremely Large Telescopes (ELTs). These instruments will be able to detect much fainter planets if the planets are sufficiently distant from their parent star to be separable from the angular size of the optical point-spread function (Clampin et al. 2001; Lardière et al. 2004; Trauger et al. 2003; Krist et al. 2003; Dekany et al. 2004; Codona & Angel 2004).

For example, Lardière et al. (2004) used detailed simulations of adaptive optics systems with different actuator pitches placed on a ground-based ELT of various aperture sizes located in varying atmospheric conditions to calculate the planet-to-star flux ratio that would be required to reach a given S/N. Generally speaking, they concluded that a 30 m diameter ELT on one of the best sites in the world (e.g., at Mauna Kea or in the Antarctic) could easily detect, with S/N = 3 and in just one night's observation, planets with brightness ratios as small as 1×10^{-9} over the range of projected planet–host star separations corresponding to $0''1$–$1''0$. These separations correspond to planets with semimajor axes $1\,\text{AU} \leq a \leq 10\,\text{AU}$ for systems 10 pc distant from Earth (and about a factor of 10 greater at 30 pc). Such planets are more likely to have the temperatures of Saturn and Jupiter and thus the scattering properties that we have assumed here. We note that a ratio of 1×10^{-9} corresponds to the purple contrast levels shown in Figure 13, indicating that over almost the entire range of orbital eccentricities, viewing angles, and scattering properties that we have considered here, planets would be detectable by such systems, even if they orbited 10 AU from their host. Many technical challenges must be overcome before contrast levels of 1×10^{-9} become detectable from the ground, but recent laboratory measurements (W. Traub 2004, private communication) have already indicated that this level of contrast is feasible for the TPF-C.

Projected onto the sky plane, a planet is most separated from its host star (and thus best spatially resolved) near half-phase, i.e., at $\Theta \sim \pm 90°$ (Figs. 6–9). Lambertian planets may overestimate the reflected light amplitudes of anisotropically scattering planets at half-phase (see Fig. 6). On the other hand, rings may increase the reflected brightness by a factor of 2–3 or more if they are larger than those of Saturn, increasing the chance of light-curve detection, as would larger planets. In this light, it is interesting to note that because planet size is not believed to grow substantially with planet mass for planets heavier than Jupiter (Guillot et al. 1996), searching for the photometric signature of large rings of extrasolar planets (if they exist) may be an easier task than searching for the planets themselves.

5. CONCLUSIONS

We have examined the effects of rings, realistic scattering properties as actually measured for Saturn and Jupiter, viewing geometry, and orbit eccentricity on the characteristics of reflected light from extrasolar planets and their combined planet–host star light curve. In particular, we have noted signatures of ringed planets and orbital eccentricity and have indicated cases in which these may be distinguished from or confused with other effects. In Table 3, we summarize several signatures that may be observed in exoplanet light curves in reflected light and indicate their generic features if caused by planetary rings, eccentric orbits, or planetary surface effects.

---

[10] We model wavelengths here that are more similar to the R passband than the V band.

TABLE 3

Signatures of Rings, Orbital Eccentricity, and Planetary Surface in the Light Curve

Signature	Rings	Eccentric Orbit	Alternative
Double peak...	Rare smooth peaks	Rare, sharp trough near one peak	Surface asymmetry[a] or seasons
Large-scale asymmetry	Common	Common	Surface asymmetry,[a] oblateness, or seasons
Light-curve fine structure	Abrupt changes	Smooth	
Shift of curve maximum from $\Theta = 0^{\circ}$ (requires radial velocity data).........................	Often	Never for circular orbit, calculable for eccentric orbits	Surface asymmetry,[a] oblateness, seasons, or backscattering[b]

[a] Planet-scale asymmetry of the brightness distribution, e.g., bright poles.
[b] The strength of the backscattering peak of the planetary phase function changes the shift of the curve maximum relative to $\Theta = 0^{\circ}$, which is known within the range of the assumed phase functions (see Fig. 12).

Our studies of planets with Jovian, Saturnian, and Lambertian scattering properties moving in eccentric orbits hold the following messages for observers:

1. An anisotropically scattering planet is considerably fainter at half-phase ($\Theta = \pm 90^{\circ}$) than is a Lambertian planet (see Fig. 6).

2. Anisotropically scattering planets are also fainter at low inclinations than are Lambertian planets.

3. For many geometries, the eccentricity of the orbit may increase the maximum amplitude of the reflected light curve by a large amount compared with that of a planet on a circular orbit with the same semimajor axis (see Fig. 13).

4. Over a wide range of possible geometries, the timing of the light-curve maximum with respect to pericenter can be used to constrain the orbital inclination and/or atmospheric backscattering properties (see Fig. 12).

5. Accounting for realistic ring scattering properties and ring shadows, rings such as those of Saturn can increase the total amplitude of the reflected light curve by factors of 2–3 (see Fig. 9).

In summary, eccentric orbits, rings, and atmospheric scattering properties of exoplanets may be detected in the next decade or so by the effects they create on the light curve of the planet's reflected light, and these effects can often be distinguished by the shape of the observed light curve.

We thank R. A. West for useful references on Jupiter's scattering. This work began at the NASA Goddard Institute for Space Studies while U. A. D. was supported by Anthony D. Del Genio under the Cassini Project.

REFERENCES

Arnold, L., & Schneider, J. 2004, A&A, 420, 1153
Baines, K. H., Carlson, R. W., & Kamp, L. W. 2002, Icarus, 159, 74
Barnes, J. W., & Fortney, J. J. 2004, ApJ, 616, 1193
Benedict, G. F., et al. 2002, ApJ, 581, L115
Bouchy, F., Pont, F., Santos, N. C., Melo, C., Mayor, M., Queloz, D., & Udry, S. 2004, A&A, 421, L13
Burrows, A., & Sharp, C. M. 1999, ApJ, 512, 843
Charbonneau, D., Brown, T. M., Latham, D. W., & Mayor, M. 2000, ApJ, 529, L45
Charbonneau, D., Noues, R., Korzennik, S., Nisenson, P., Jha, S., Vogt, S., & Kibrick, R. I. 1999, ApJ, 522, L145
Clampin, M., et al. 2001, BAAS, 33, 1356
Codona, J. L., & Angel, R. 2004, ApJ, 604, L117
Collier Cameron, A., Horne, K., Penny, A., & Leigh, C. 2002, MNRAS, 330, 187
Dekany, R., Stapelfeldt, K., Traub, W., Macintosh, B., Woolf, N., Colavita, M., Trauger, J., & Ftaclas, C. 2004, PASP, submitted
Dones, L., Cuzzi, J., & Showalter, M. 1993, Icarus, 105, 184
Green, D., Matthews, J., Seager, S., & Kuschnig, R. 2003, ApJ, 597, 590
Guillot, T., Burrows, A., Hubbard, W. B., Lunine, J. I., & Saumon, D. 1996, ApJ, 459, L35
Hatzes, A. P. 2003, in ASP Conf. Ser. 294, Scientific Frontiers in Research on Extrasolar Planets, ed. D. Deming & S. Seager (San Francisco: ASP), 523
Henry, G. W., Marcy, G. W., Butler, R. P., & Vogt, S. S. 2000, ApJ, 529, L41
Jenkins, J. M., & Doyle, L. R. 2003, ApJ, 595, 429
Jenkins, J. M., Witteborn, F., Koch, D. G., Dunham, E. W., Borucki, W. J., Updike, T. F., Skinner, M. A., & Jordan, S. P. 2000, Proc. SPIE, 4013, 520
Karkoschka, E. 1994, Icarus, 111, 174
———. 1998, Icarus, 133, 134
Koch, D. G., Borucki, W. J., Dunham, E. W., Jenkins, J. M., Webster, L., & Witteborn, F. 2000, Proc. SPIE, 4013, 508
Konacki, M., Torres, G., Jha, S., & Sasselov, D. 2003, Nature, 421, 507

Konacki, M., et al. 2004, ApJ, 609, L37
Krist, J. E., Clampin, M., Petro, L., Woodruff, R. A., Ford, H. C., Illingworth, G. D., & Ftaclas, C. 2003, Proc. SPIE, 4860, 288
Lardière, O., Salinari, P., Jolissaint, L., Carbillet, M., Riccardi, A., & Esposito, S. 2004, Proc. SPIE, 5382, 550
Leigh, C., Collier Cameron, A., Horne, K., Penny, A., & James, D. 2003a, MNRAS, 344, 1271
Leigh, C., Collier Cameron, A., Udry, S., Donati, J., Horne, K., James, D., & Penny, A. 2003b, MNRAS, 346, L16
Mekler, Y., & Podolak, M. 1994, Planet. Space Sci., 42, 865
Murray, C. D., & Dermott, S. F. 2001, Solar System Dynamics (Cambridge University Press)
Pepe, F., Mayor, M., Galland, F., Naef, D., Queloz, D., Santos, N., Udry, S., & Burnet, M. 2002, A&A, 388, 632
Remund, Q. P., Jordan, S. P., Updike, T. F., Jenkins, J. M., & Borucki, W. J. 2002, Proc. SPIE, 4495, 182
Seager, S., Whitney, B., & Sasselov, D. 2000, ApJ, 540, 504
Simon-Miller, A. A., Conrath, B. J., Gierasch, P. J., & Beebe, R. F. 2000, Icarus, 145, 454
Smith, P. H., & Tomasko, M. G. 1984, Icarus, 58, 35
Sudarsky, D., Burrows, A., & Hubeny, I. 2003, ApJ, 588, 1121
Sudarsky, D., Burrows, A., & Pinto, P. 2000, ApJ, 538, 885
Tomasko, M. G., & Doose, L. R. 1984, Icarus, 58, 1
Tomasko, M. G., West, R. A., & Castillo, N. D. 1978, Icarus, 33, 558
Trauger, J., et al. 2003, BAAS, 203, 0303
Udalski, A., Pietrzynski, G., Szymanski, M., Kubiak, M., Zebrun, K., Soszynski, I., Szewczyk, O., & Wyrzykowski, L. 2003, Acta Astron., 53, 133
Udalski, A., Zebrun, K., Szymanski, M., Kubiak, M., Soszynski, I., Szewczyk, O., Wyrzykowski, L., & Pietrzynski, G. 2002a, Acta Astron., 52, 115
Udalski, A., et al. 2002b, Acta Astron., 52, 1
Walker, G., et al. 2003, PASP, 115, 1023
Weidenschilling, S. J., & Lewis, J. S. 1973, Icarus, 20, 465